

JOINT DESMOKING, SPECULARITY REMOVAL, AND DENOISING OF LAPAROSCOPY IMAGES VIA GRAPHICAL MODELS AND BAYESIAN INFERENCE

Ayush Baid¹, Alankar Kotwal¹, Riddhish Bhalodia², S. N. Merchant¹, Suyash P. Awate^{1*}

¹ Indian Institute of Technology (IIT) Bombay.

² University of Utah.

ABSTRACT

Laparoscopic images exhibit artifacts resulting from surgical smoke, specular highlights, and noise. These artifacts degrade the results of subsequent processing (e.g., tracking, segmentation, and depth analysis) and compromise surgical quality. We formulate a *unified Bayesian inference problem* for desmoking, specularity removal, and denoising in laparoscopic images. We propose novel *probabilistic graphical models* and *sparse dictionary models* as image priors. For inference, we rely on *variational Bayesian expectation maximization*. Results on simulated and real-world laparoscopic images, including clinical expert evaluation, show that our joint optimization method outperforms the state of the art.

Index Terms— Laparoscopy, desmoking, specularity removal, denoising, variational Bayes, EM, graphical models.

1. INTRODUCTION AND RELATED WORK

Laparoscopy images [1] can get severely corrupted with specular highlights [2, 3], surgical smoke [4], and noise. These artifacts degrade the efficacy of the subsequent image processing for tracking [5, 6], segmentation [7, 8], depth analysis [9, 10, 2], and augmented reality [11]. The literature on laparoscopic image processing presents some specularity-removal methods [12, 2, 3], but desmoking methods are obscure [13]. We propose a *unified formulation* for joint desmoking, specularity removal, and denoising of laparoscopic images.

Typical methods [12, 3] for specularity removal in laparoscopic images rely on inpainting using isotropic diffusion that models neither edges nor texture, e.g., created by blood vessels, leading to oversmoothing at the specularities. [2] relies on spatiotemporal registration and removes highlights by averaging in neighborhoods determined by the control points underlying the deformation; this averaging cannot model texture well. In contrast, we use a *patch-based dictionary model* for inpainting, and denoising (early works on patch-based denoising are in [14, 15, 16]), to preserve natural texture.

Desmoking in laparoscopic images is akin to dehazing in landscape images. However, while haze, caused by fog, is dictated by scene depth, smoke concentration can vary independent of depth. Early dehazing methods [17, 18] employ

Markov random field (MRF) models on the depth-dependent transmission map, but, unlike our method, ignore prior models on color probability density functions (PDFs) and textures of uncorrupted images. Later dehazing methods [19, 20] rely on a dark-channel prior on the uncorrupted image colors and use it to estimate the transmission map via soft matting or guided filtering. The underlying sequential-estimation schemes fail to employ the estimated hazeless image to improve the transmission-map estimate. None of these methods [17, 18, 19, 20] remove specularities and noise.

Later methods [21, 22, 13, 23, 24] perform denoising and dehazing both, but ignore specularity removal. While [21] uses a dark-channel prior, its focus on real-time processing prevents the use of edge / texture preserving priors on the uncorrupted image. [22] uses repeated acquisition that is impractical in laparoscopy. [23] uses heuristics to iteratively solve dehazing and denoising, without treating both as a joint estimation problem and losing convergence guarantees for the iterations. The defogging in [24] uses MRF priors on depth and chromaticity, but, by ignoring priors on colors and texture, it depicts results [24] with unnatural colors and illumination. The method in [13], unlike our method, does *not* use a texture preserving prior, uses a correlated color space that models color-channel PDF priors less effectively, and uses mode approximation for the transmission-map latent variable.

This paper proposes a unified Bayesian formulation for the tasks of desmoking, specularity removal, and denoising in laparoscopy images. Unlike sequential schemes, our joint formulation seamlessly and rigorously integrates information across tasks. We use novel priors to preserve natural image color and texture, relying on probabilistic graphical models and sparse dictionaries. Unlike past methods, our inference accounts for the variability in the latent transmission map via variational Bayes (VB) expectation maximization (EM). Results on simulated and clinical data, including clinical expert evaluation, show that our joint VBEM inference improves estimates of uncorrupted images, over the state of the art.

2. METHODS

This section details our novel probabilistic graphical modeling and inference. We denote random variables by uppercase letters and their specific instances by the lowercase letters.

*We thank funding via the IIT Bombay Seed Grant 14IRCCSG010.

Uncorrupted-Image Model. The *unknown uncorrupted image* appears piecewise textured, where the pieces correspond to anatomical structures or surgical instruments. The restricted imaging environment (i.e., inside the human body) imparts characteristic colors and textures to the scene. We model colors, textures, and regularity underlying the uncorrupted image, comprising I pixels, by a MRF $\mathbf{X} := \{X_i\}_{i=1}^I$, where, at each pixel i , the random variable X_i is vector valued (3-vector for 3 color components). For the MRF, we define a neighborhood system $\mathcal{N} := \{\mathcal{N}_i\}_{i=1}^I$, where \mathcal{N}_i is the set of neighbor pixels for pixel i . We design the MRF prior on \mathbf{X} to model (i) pixel color statistics and contrast and (ii) patch color statistics to capture texture and spatial regularity.

We model pixel color statistics in a perception-based data-adaptive decorrelated color space [25] with one achromatic channel (c_1) and two chromatic channels ($c_2 c_3$). We use a set of high-quality (virtually, uncorrupted) images to learn the PDF of each color channel. We propose to model the achromatic-channel PDF as gamma ($\Gamma_1(\cdot)$) and the other two chromatic-channel PDFs as Gaussian ($G_2(\cdot), G_3(\cdot)$), which leads to good fits (Figure 1). We design the prior on the color components to penalize the deviation between the learned cumulative distribution functions (CDFs) $F^{\Gamma_1 G_2 G_3}$ and the color component CDFs ($F_{c_1}^{\mathbf{x}}(\cdot), F_{c_2}^{\mathbf{x}}(\cdot), F_{c_3}^{\mathbf{x}}(\cdot)$) in the uncorrupted image estimate \mathbf{x} . We penalize the Kolmogorov-Smirnov (KS) distance between the CDFs: $\text{KS}(F^{\Gamma_1 G_2 G_3}, F^{\mathbf{x}}) := \text{KS}(F_{c_1}^{\Gamma_1}, F_{c_1}^{\mathbf{x}}) + \text{KS}(F_{c_2}^{G_2}, F_{c_2}^{\mathbf{x}}) + \text{KS}(F_{c_3}^{G_3}, F_{c_3}^{\mathbf{x}})$. We model KS distance as a MRF potential function using a fully-connected pixel-neighborhood system \mathcal{N} with a potential function on the clique of all pixels.

We model texture and enforce spatial regularity by using a sparse dictionary model on image patches. We penalize the deviation (squared norm of difference) of each $n \times n$ patch, in the uncorrupted image \mathbf{x} , from its sparse dictionary fit. We model this in our MRF framework by using a potential function on cliques of square neighborhoods of size $m \times m$, where $m := 2n - 1$, around each pixel. Given a learned dictionary \mathbf{D} , for each square neighborhood \mathbf{x}_i^m around pixel i , the MRF potential function (penalty) is $(\min_{s_i} \|\mathbf{x}_i^m - \mathbf{D}s_i\|_2^2 + \lambda \|s_i\|_1)$, where s_i is the coefficient vector used to represent patch \mathbf{x}_i^m . We regularize the L_1 norm as the Huber loss function.

So, our prior on the uncorrupted image \mathbf{X} is $P(\mathbf{X}) := \exp(-E(\mathbf{X}))/Z$, with Gibbs energy $E(\mathbf{X}) := \alpha \text{KS}(F^{\Gamma_1 G_2 G_3}, F^{\mathbf{x}}) + \sum_{i=1}^I \beta (\min_{s_i} \|\mathbf{x}_i^m - \mathbf{D}s_i\|_2^2 + \lambda \|s_i\|_1)$, partition function Z , and free parameters $\alpha, \beta, \lambda \in \mathbb{R}^+$.

Image Degradation Model. The acquired laparoscopic image \mathbf{Y} is a degraded version of \mathbf{X} because of (a) specular white highlights, (b) surgical smoke colored bright gray, and (c) random noise due to low-light imaging and sensor errors, all of which degrade post-processing for surgical vision [1].

We model specular highlighting on the image \mathbf{X} by the replacement of the colors of the affected pixels to that of the incident white light of the laparoscopic camera. Thus, each pixel in the image \mathbf{Z} corrupted with specular highlights is

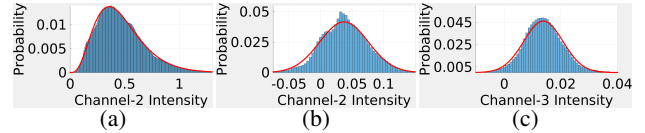


Fig. 1. Learning Prior PDFs on Color. Empirical histograms (bar plots) and fitted parametric PDFs (solid curves) in uncorrupted laparoscopic images, for 3 channel components: (a) gamma Γ_1 , (b) Gaussian G_2 , (c) Gaussian G_3 .

modeled by $Z_i := (1 - R_i)X_i + R_iK$, where K is the color white and \mathbf{R} is an indicator map (image) such that $R_i = 1$ iff pixel i exhibits specular reflection; otherwise $R_i = 0$. The image \mathbf{R} is typically very sparse and has spatial regularity.

We model the effects of surgical smoke on the image \mathbf{Z} by a convex weighted combination of the image color Z_i and the smoke color S . The image of weights is the *transmission map*, modeled by a MRF $\mathbf{T} := \{T_i\}_{i=1}^I$ where the random variables T_i take real values within $[0, 1]$. For this MRF \mathbf{T} , we define a neighborhood system $\mathcal{N}^T := \{\mathcal{N}_i^T\}_{i=1}^I$, where the set \mathcal{N}_i^T is the set of neighboring pixels for pixel i . We assume the transmission map to be spatially smooth, where its values vary with smoke concentration and scene depth. So, we model $P(\mathbf{T}) := (1/W) \exp(-B(\mathbf{T}))$ with partition function W and Gibbs energy $B(\mathbf{T}) := \sum_{i=1}^I \sum_{j \in \mathcal{N}_i^T} \gamma(T_i - T_j)^2$, with free parameter $\gamma \in \mathbb{R}^+$. At pixel i , the image color corrupted with speckles and smoke is $T_i Z_i + (1 - T_i)S$, where $T_i Z_i$ is the direct attenuation due to the loss in scene radiance and $(1 - T_i)S$ is the contribution due to scattered light.

The color at each pixel in the acquired image $\mathbf{Y} := \{Y_i\}_{i=1}^I$ is also corrupted by independent and identically distributed random noise that we model as additive Gaussian. Thus, $Y_i := T_i Z_i + S(1 - T_i) + \eta_i$, where $\eta_i \sim G(0, \sigma^2)$.

Problem Formulation. We formulate laparoscopic image specularity removal, desmoking, and denoising as a *unified* Bayesian estimation problem. The speckle color K and the smoke color S are known to be very close to white, which is the color of the light used during imaging; thus, we set s and k to white. Given the corrupted image \mathbf{y} , we first find a robust estimate of the specular-highlight regions \mathbf{R} . Then, we estimate the uncorrupted image \mathbf{x} by treating the transmission map \mathbf{T} as a latent variable and using VBEM optimization.

At the pixels with specular highlights, i.e., where $R_i = 1$, the data acquisition is uninformative because the intensities are typically saturated. Thus, knowing \mathbf{r} , we discard such pixels from the observed image \mathbf{y} to produce an image $\hat{\mathbf{y}}$ with holes, where colors $\hat{y}_i := y_i$ at all pixels i without specularities. Thus, treating the image with holes, i.e., $\hat{\mathbf{y}}$, as data, the data likelihood is $P(\hat{\mathbf{y}}|\mathbf{x}, \mathbf{r}, \mathbf{t}) := \prod_{\{i|r_i=0\}} G(y_i; t_i x_i + (1 - t_i)s, \sigma^2)$. We then rely on the prior on \mathbf{X} to inpaint holes, while maintaining fidelity and spatial regularity with the pixel colors around the holes.

Our maximum-a-posteriori (MAP) estimate of the uncorrupted image is $\hat{\mathbf{x}} := \arg \max_{\mathbf{x}} P(\mathbf{x}|\hat{\mathbf{y}}, \mathbf{r})$. Given that im-

ages $\mathbf{X}, \mathbf{R}, \mathbf{T}$ are independent of each other, the posterior $P(\mathbf{x}|\hat{\mathbf{y}}, \mathbf{r}) \propto P(\hat{\mathbf{y}}|\mathbf{x}, \mathbf{r})P(\mathbf{x}) = \int_t P(\hat{\mathbf{y}}, \mathbf{t}|\mathbf{x}, \mathbf{r})P(\mathbf{x})dt = \int_t P(\hat{\mathbf{y}}|\mathbf{t}, \mathbf{x}, \mathbf{r})P(\mathbf{t})P(\mathbf{x})dt$, where the first term is the data likelihood and the other terms are priors on images \mathbf{X} and \mathbf{T} .

Estimating R: Regions with Specular Highlights. We process conservatively to detect all reasonably sized highlights. We estimate \mathbf{R} by (i) selecting pixels with colors close to white, (ii) using connected component analysis to exclude regions larger than 40 mm^2 , to safeguard against misdetecting white instruments as highlights, and (iii) regularizing regions by morphological opening (to remove tiny regions) followed by closing (to remove tiny holes within regions) using a disc structuring element of diameter around 1 mm.

VBEM Optimization. The EM algorithm entails iterative optimization over the uncorrupted image \mathbf{x} . At iteration m , with estimate \mathbf{x}^m , the E step defines the function $Q(\mathbf{x}; \mathbf{x}^m) := E_{P(\mathbf{T}|\hat{\mathbf{y}}, \mathbf{x}^m)} [\log P(\hat{\mathbf{y}}, \mathbf{T}|\mathbf{x}, \mathbf{r})P(\mathbf{x})] = P(\mathbf{x})E_{P(\mathbf{T}|\hat{\mathbf{y}}, \mathbf{x}^m)} [\log P(\hat{\mathbf{y}}, \mathbf{T}|\mathbf{x}, \mathbf{r})]$ and the M step updates the estimate as $\mathbf{x}^{m+1} := \arg \max_{\mathbf{x}} Q(\mathbf{x}; \mathbf{x}^m)$.

In the E step, the expectation is analytically intractable. So, we use a variational approximation for $P(\mathbf{T}|\hat{\mathbf{y}}, \mathbf{x}^m)$ as a product of pixel-wise factors $\prod_i F_i(T_i|\hat{\mathbf{y}}, \mathbf{x}^m)$, where each factor is Gaussian with mean μ_i and variance σ_i^2 (we assume $\sigma \ll 1$). VBEM then (i) optimizes these factors, i.e., parameters $\{\mu_i\}$ and $\{\sigma_i^2\}$, to best fit the PDF $P(\mathbf{T}|\hat{\mathbf{y}}, \mathbf{x}^m)$ and (ii) uses the optimal factorization to evaluate the expectation.

VBEM optimizes factors $F_i(T_i) := G(\mu_i, \sigma_i^2)$ iteratively. The optimal factor at pixel i , keeping all other factors fixed, is $F_i^*(T_i|\hat{\mathbf{y}}, \mathbf{x}^m) \propto \exp(E_{\prod_{j \neq i} F_j^*(T_j)} [\log P(\hat{\mathbf{y}}, \mathbf{T}|\mathbf{x})])$. Because of our design, $\log P(\hat{\mathbf{y}}, \mathbf{T}|\mathbf{x}) = \sum_{\{i|R_i=0\}} (y_i - T_i x_i - (1 - T_i)s)^2 / \sigma^2 + \sum_i \sum_{j \in \mathcal{N}_i^T} \gamma(T_i - T_j)^2$ is a quadratic function in each T_j . Thus, the expectation of this quadratic function in T_j with respect to individual Gaussian distributions over T_j replaces linear terms T_j with μ_j and square terms T_j^2 with $\mu_j^2 + \sigma_j^2$. This expectation is now a quadratic function of T_i alone, and we use completion of squares to write it as $-0.5(T_i - \mu_i^*)^2 / \sigma_i^{*2} + \delta$, where δ is independent of T_i and gets absorbed into the normalization constant of $F_i(T_i)$. So, the optimal factor $F_i^*(T_i) = G(\mu_i^*, \sigma_i^{*2})$.

After optimizing all factors, we minimize $-\log Q(\mathbf{x}; \mathbf{x}^m) = -\log P(\mathbf{x}) + \sum_{\{i|R_i=0\}} (0.5/\sigma_i^2)((\mu_i^{*2} + \sigma_i^{*2})(x_i - s)^2 - 2(y_i - s)\mu_i(x_i - s)) + \delta'$, where δ' is independent of \mathbf{x} . We optimize using gradient descent, with adaptive step size to ensure that each update increases the log posterior. We replace the gradient of the KS distance by the difference between the current estimated x and its CDF-transformed image that matches its color-component histograms to the prior color-component histograms. We use a maximum-likelihood estimate for the noise variance σ^2 using a small image patch with roughly constant intensity. We tune the free parameters $\alpha, \beta, \lambda, \gamma$ empirically (just once for all experiments in the paper); Section 3 shows the results are robust to the choice of values for the free parameters.

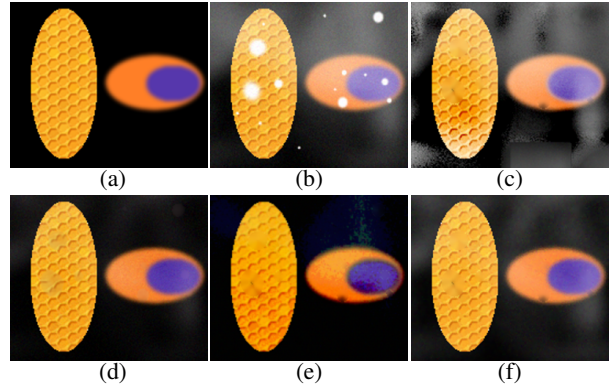


Fig. 2. Validation on Simulated Data. (a) Phantom (color component values $\in [0, 255]$). (b) Corrupted phantom with smoke, specularities, and low noise ($\sigma = 5$). Results of processing image (b), using: (c) adaptive filtering [21] followed by inpainting; (d) *our method*; (e) denoising and desmoking [13] followed by inpainting; (f) denoising [26] followed by dehazing [19] followed by inpainting.

3. VALIDATION AND RESULTS

We perform quantitative and qualitative evaluation on (i) simulated data and (ii) real-world laparoscopic images obtained from (hamlyn.doc.ic.ac.uk/vision) [6] and our clinical collaborators. We evaluate 3 other state-of-the-art algorithms that perform the tasks of dehazing / desmoking, specularity removal, and denoising. To the best of our knowledge, ours is the first unified algorithm for these 3 tasks.

Validation on Simulated Data. We simulate phantom images and corrupt them with specularities, smoke, and noise. We evaluate (i) our joint estimation method, (ii) desmoking and denoising via [13] followed by specularity removal for which we choose to inpaint using anisotropic diffusion that is better than isotropic diffusion used in [12, 3], (iii) adaptive filtering [21] followed by inpainting, and (iv) denoising (we choose the edge-preserving bilateral filter [26]) followed by dehazing [19]—the strategy mentioned in [22, 23]—and subsequently inpainting. We measure performance using the relative root mean square error (RRMSE): $\|\hat{\mathbf{x}} - \mathbf{x}\|_F / \|\mathbf{x}\|_F$ between the ground truth \mathbf{x} and its estimate $\hat{\mathbf{x}}$. Qualitative (Figure 2) and quantitative (Figure 4(a),(c)) evaluation proves our method to consistently better preserve natural texture, color, and contrast, as well as reduce smoke, specularity, and noise. This stems from our sparse dictionary prior on patches and distribution prior on the decorrelated color space.

Validation on High-Quality Laparoscopic Images. We select 24 high-quality images as ground truth, corrupt them, and evaluate methods qualitatively (Figure 3) and quantitatively (Figure 4(b),(d)). Figure 5(a) shows our learned dictionary from the 24 high-quality images. Estimated uncorrupted images using our method have significantly smaller RRMSE and more accurate texture and colors. Other methods produce unnatural hues and low contrast (absence of color distribution

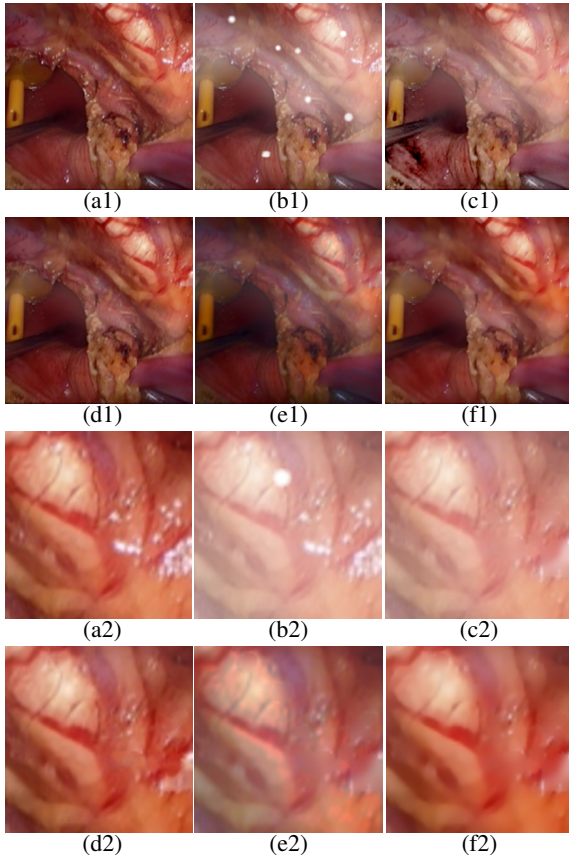


Fig. 3. Validation on High-Quality Laparoscopic Images. **(a1)** Ground truth. **(b1)** Corrupted. Results of processing image (b1), using: **(c1)** adaptive filtering [21] followed by inpainting; **(d1)** our method; **(e1)** denoising and desmoking [13] followed by inpainting; **(f1)** denoising [26] followed by dehazing [19] followed by inpainting. **(a2)–(f2)** Zoomed insets.

prior) and oversmoothing that is exemplified in inpainting the specularities (absence of a texture-preserving prior).

Robustness of Results to Parameter Tuning. The free parameters number: (i) 6 for sequential specularity removal, dehazing, and denoising, (ii) 4 ($\alpha, \beta, \lambda, \gamma$) for our method, and (iii) 2 for adaptive filtering followed by inpainting. We repeat quantitative analysis by randomly perturbing the parameter values within $\pm 10\%$ of the empirically-tuned values; the plots (Figure 4(b)–(d)) remain virtually unchanged.

Results on Corrupted Laparoscopic Images. We select laparoscopic images with a high amount of specularity and smoke. Figure 5 shows that, unlike our method, other methods oversmooth the entire image (including within the specularity) and show lower contrast and more smoke.

Clinical Evaluation. We perform a blind evaluation by 4 experts who rated each processed image on a scale of 1 (poor) to 4 (excellent). The mode, median, mean, and SD of the ratings for (i) our method were 4, 4, 3.9, and 0.3, and (ii) the next best method, i.e., [13] followed by inpainting, were 3, 3, 2.9, and 0.4, respectively. Our method gives statistically

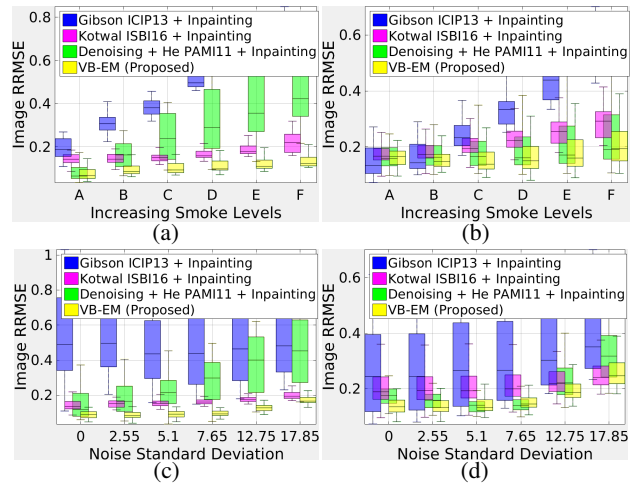


Fig. 4. Validation on Simulated and High-Quality Laparoscopy Images. Box plots for RRMSE (defined in text), for a fixed moderate noise level and *varying smoke levels*, with 50 simulated runs per level, for **(a)** phantom, **(b)** a set of 24 high-quality laparoscopic images. Similar box plots, for a fixed moderate smoke level and *varying noise levels*, for **(c)** phantom, **(d)** a set of 24 high-quality laparoscopic images.

significantly better ratings; p -value $< 10^{-35}$ for a Pearson's chi-square 2-sample test on the categorical distributions.

Conclusion. We propose a unified Bayesian formulation for specularity removal, desmoking, and denoising laparoscopic images, using (i) sparse dictionaries, probabilistic graphical models, and VBEM inference, and (ii) priors on patch colors and pixel colors to preserve natural texture and contrast. Qualitative, quantitative, and clinical evaluation, shows that our method outperforms over the state of the art.

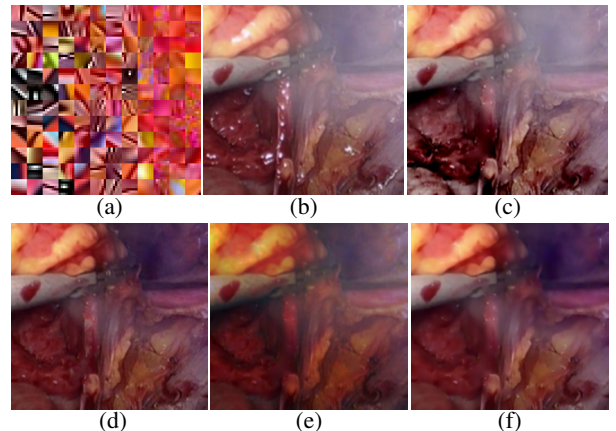


Fig. 5. Results on Corrupted Laparoscopic Images. **(a)** Learned dictionary atom examples. **(b)** Corrupted image. Results of processing image (b) using: **(c)** adaptive filtering [21] followed by inpainting; **(d)** our method; **(e)** denoising and desmoking [13] followed by inpainting; **(f)** denoising [26] followed by dehazing [19] followed by inpainting.

4. REFERENCES

- [1] D Stoyanov, “Surgical vision,” *Ann. Biomed. Engg.*, vol. 40, no. 2, pp. 332–45, 2012.
- [2] D Stoyanov and G Yang, “Removing specular reflection components for robotic assisted laparoscopic surgery,” in *Int. Conf. Imag. Proc. (ICIP)*, 2005, pp. 632–5.
- [3] C-A Saint-Pierre, J Boisvert, G Grimard, and F Cheriet, “Detection and correction of specular reflections for automatic surgical tool segmentation in thoracoscopic images,” *Machine Vision Appl.*, vol. 22, pp. 171–80, 2007.
- [4] W Barrett and S Garber, “Surgical smoke: A review of the literature. Is this just a lot of hot air?,” *Surgical Endoscopy*, vol. 17, no. 6, pp. 979–87, 2003.
- [5] R Wolf, J Duchateau, P Cinquin, and S Voros, “3D tracking of laparoscopic instruments using statistical and geometric modeling,” in *Proc. Med. Imag. Comp. Comput. Assist. Interv. (MICCAI)*, 2011, pp. 203–210.
- [6] S Giannarou, M Visentini-Scarzanella, and G-Z Yang, “Probabilistic tracking of affine-invariant anisotropic regions,” *IEEE Trans. Pattern Anal. Mach. Intell. (TPAMI)*, vol. 35, no. 1, pp. 130–43, 2013.
- [7] K Prokopetc, T Collins, and A Bartoli, “Automatic detection of the uterus and fallopian tube junctions in laparoscopic images,” in *Info. Proc. Med. Imag. (IPMI)*, 2015, pp. 552–63.
- [8] S Voros, E Orvain, P Cinquin, and J Long, “Automatic detection of instruments in laparoscopic images: a first step towards high level command of robotized endoscopic holders,” in *IEEE Int. Conf. Biomed. Robotics Biomechatronics*, 2006, pp. 1107–12.
- [9] L Maier-Hein, A Groch, Alberto Bartoli, S Bodenstedt, G Boissonnat, P-L Chang, NT Clancy, DS Elson, S Haase, E Heim, Joachim Hornegger, P Jannin, H Kenngott, T Kilgus, H-P Schlemmer, A Seitel, S Speidel, Michael Wagner, and D Stoyanov, “Comparative validation of single-shot optical techniques for laparoscopic 3-D surface reconstruction,” *IEEE Trans. Med. Imag. (TMI)*, vol. 33, no. 10, pp. 1913–1930, 2014.
- [10] L Maier-Hein, P Mountney, A Bartoli, H Elhawary, D Elson, A Groch, A Kolb, M Rodrigues, J Sorger, S Speidel, and D Stoyanov, “Optical techniques for 3D surface reconstruction in computer-assisted laparoscopic surgery,” *Med. Imag. Anal. (MedIA)*, vol. 17, no. 8, pp. 974–996, 2013.
- [11] P Mountney, J Fallert, S Nicolau, L Soler, and P Mewes, “An augmented reality framework for soft tissue surgery,” in *Int. Conf. Med. Imag. Comp. Comput. Assist. Interv. (MICCAI)*, 2014, pp. 423–431.
- [12] M Arnold, A Ghosh, S Ameling, and G Lacey, “Automatic segmentation and inpainting of specular highlights for endoscopic imaging,” *EURASIP J. Imag. Video Proc.*, pp. 1–12, 2010.
- [13] A Kotwal, R Bhalodia, and S P Awate, “Joint desmoking and denoising of laparoscopy images,” in *Proc. IEEE Symp. Biomed. Imag. (ISBI)*, 2015, pp. 1050–4.
- [14] A Buades, B Coll, and J-M Morel, “A non-local algorithm for image denoising,” in *IEEE Int. Conf. Comp. Vis. Pattern Recog.*, 2005, vol. 2, pp. 60–65.
- [15] S P Awate and R T Whitaker, “Higher-order image statistics for unsupervised, information-theoretic, adaptive, image filtering,” in *IEEE Int. Conf. Comp. Vis. Pattern Recog.*, 2005, vol. 2, pp. 44–51.
- [16] S P Awate and R T Whitaker, “Feature-preserving MRI denoising: A nonparametric empirical-Bayes approach,” *IEEE Trans. Med. Imag.*, vol. 26, no. 9, pp. 1242–1255, 2007.
- [17] R Fattal, “Single image dehazing,” *ACM Trans. Graphics*, vol. 34, no. 1, 2008.
- [18] R Tan, “Visibility in bad weather from a single image,” in *Proc. IEEE Int. Conf. Comp. Vis. Pattern Recog. (CVPR)*, 2008, pp. 1–8.
- [19] K He, J Sun, and X Tang, “Single image dehazing using dark channel prior,” in *Proc. IEEE Int. Conf. Comp. Vis. Pattern Recog. (CVPR)*, 2009, pp. 1956–63.
- [20] J Pang, O Au, and Z Guo, “Improved single image dehazing using guided filter,” in *Asia Pacific Signal Info. Proc. Assoc. Annual Summit and Conf.*, 2011.
- [21] K Gibson and T Nguyen, “Fast single image fog removal using the adaptive Wiener filter,” in *Proc. IEEE Int. Conf. Imag. Proc. (ICIP)*, 2013, pp. 714–18.
- [22] N Joshi and M Cohen, “Seeing Mt. Rainier: Lucky imaging for multi-image denoising, sharpening, and haze removal,” in *Proc. IEEE Int. Conf. Comp. Photography (ICCP)*, 2010, pp. 1–8.
- [23] E Matlin and P Milanfar, “Removal of haze and noise from a single image,” in *SPIE Optics Photonics*, 2012.
- [24] K Nishino, L Kratz, and S Lombardi, “Bayesian defogging,” *Int. J. Comp. Vis.*, vol. 98, pp. 263–278, 2012.
- [25] E Reinhard, M Ashikhmin, B Gooch, and P Shirley, “Color transfer between images,” *Applied Perception*, pp. 34–41, 2001.
- [26] C Tomasi and R Manduchi, “Bilateral filtering for gray and color images,” in *Proc. Int. Conf. Comp. Vision (ICCV)*, 1998, pp. 839–846.